

# L2R: Low-Rank and Lipschitz-Controlled Routing for Mixture-of-Experts

Minghao Yang<sup>1</sup> Ren Togo<sup>1</sup> Guang Li<sup>1</sup> Takahiro Ogawa<sup>1</sup> Miki Haseyama<sup>1</sup>  
 Email: {yang, togo, guang, ogawa, mhaseyama}@lmd.ist.hokudai.ac.jp

## Abstract

Mixture-of-Experts (MoE) models scale neural networks by conditionally activating a small subset of experts, where the router plays a central role in determining expert specialization and overall model performance. However, many modern MoE systems still adopt linear routers in raw high-dimensional representation spaces, where representation mismatch, angular concentration, and scale-sensitive scoring can jointly undermine routing discriminability and stable expert specialization. In this work, we propose Low-rank & Lipschitz-controlled Routing (L2R), a unified routing framework that reshapes both the routing space and scoring geometry. L2R performs expert assignment in a shared low-rank latent routing space and introduces Saturated Inner-Product Scoring (SIPS) to explicitly control the Lipschitz behavior of routing functions, yielding smoother and more stable routing geometry. In addition, L2R incorporates a parameter-efficient multi-anchor routing mechanism to enhance expert expressiveness. Extensive experiments on a large-scale language MoE model and a vision MoE setting on ImageNet demonstrate that L2R consistently improves routing stability, expert specialization, and overall model performance.

## 1. Introduction

Mixture-of-Experts (MoE) has emerged as a leading paradigm for scaling deep neural networks across a wide range of domains, including large language models (LLMs) (Muennighoff et al., 2025; Dai et al., 2024; Jiang et al., 2024; Yang et al., 2024) and vision backbones (Riquelme et al., 2021; Chen et al., 2023; Yang et al., 2025). By enabling conditional computation, MoE decouples model capacity from inference cost and is designed to

<sup>1</sup>Hokkaido University, Sapporo, Japan. Correspondence to: Guang Li <guang@lmd.ist.hokudai.ac.jp>.

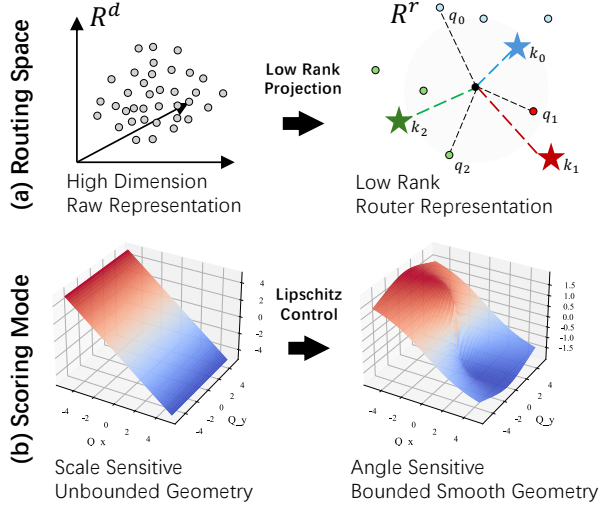


**Figure 1. Comparison between the linear router (left) and the proposed L2R framework (right).** (a) Routing space: Tokens are projected from high-dimensional raw representations into a low-rank routing space as  $q$ , where experts are represented by learnable anchors  $k$ . (b) Scoring mode: Compared to dot-product scoring, SIPS reshapes the score landscape into a bounded and smoother geometry, improving routing stability and expert specialization.

realize meaningful expert specialization (Cai et al., 2025). Central to achieving this objective is the router. As the mechanism that assigns tokens to experts under sparse and dynamic activation, the router effectively defines the functional topology of the model, governing how capacity is allocated and coordinated. Consequently, the quality of routing is a fundamental factor that determines the expressiveness, stability, and upper performance bound of MoE models (Dikkala et al., 2023).

Despite its central role, routing in modern MoE models, including OLMoE (Muennighoff et al., 2025), Mixtral (Jiang et al., 2024), Qwen2-MoE (Yang et al., 2024), and DeepSeek-MoE (Dai et al., 2024), still relies on linear routers operating directly on raw token representations. Recent efforts started to revisit this design from different perspectives. Router Upcycling (Ran et al., 2025) proposes a mixture-of-routers paradigm by initializing multiple routers from attention heads, Yuan 2.0-M32 (Wu et al., 2024a) introduces attention-based routing to enrich routing capacity, and

X-MoE (Chi et al., 2022) reveals representation collapse and token clustering induced by high-dimensional gating.

Despite these advances, modern MoE routing still exhibits two fundamental limitations: 1) **Raw-space routing and high-dimensional concentration:** Routing is typically performed in raw, high-dimensional representation spaces that are optimized for representation learning rather than expert discrimination, resulting in a fundamental representation mismatch. Moreover, in high-dimensional spaces, similarities tend to concentrate (Cai et al., 2013), reducing effective separability among experts (Chi et al., 2022). 2) **Scale-sensitive dot-product scoring:** Standard dot-product logits entangle directional alignment with feature scale, making routing highly sensitive to magnitude variations and encouraging norm-dominated competition among expert anchors, which introduces ambiguity in expert selection and weakens expert specialization.

To address these issues, we propose **Low-rank & Lipschitz-controlled Routing (L2R)**, a unified routing framework with three components: a low-rank routing space for representation decoupling, a Lipschitz-controlled scoring function for stable expert selection, and a parameter-efficient multi-anchor mechanism for enhanced expert expressiveness. **First**, instead of performing expert selection directly in the raw high-dimensional representation space, tokens are mapped into a shared low-rank routing space that produces routing-specific queries. Experts are represented by learnable anchors in this latent space, and routing is performed by matching queries to anchors. This design decouples routing from representation learning, compresses the search space for expert positioning, and alleviates geometric concentration in high-dimensional routing. **Second**, Saturated Inner-Product Scoring (SIPS) is introduced to bound the sensitivity of routing scores to representation scale and perturbations, thereby explicitly controlling the Lipschitz behavior of the routing function. By reshaping the score landscape into a smoother and more stable geometry, SIPS reduces routing ambiguity and promotes robust expert specialization. **Finally**, we develop a parameter-efficient multi-anchor routing mechanism that associates each expert with multiple anchors, allowing a single expert to capture diverse semantic views without incurring prohibitive overhead.

We extensively evaluate the proposed L2R framework across diverse MoE settings to demonstrate its generality and effectiveness. Specifically, we conduct from-scratch training on large-scale language MoE models based on OLMoE (Muenennighoff et al., 2025) and evaluate vision MoE architectures on ImageNet using ViT backbones. Across both domains, our method consistently improves routing stability, expert specialization, and overall model performance, validating its effectiveness in both language and vision domains.

Our contributions are summarized as follows:

- We identify two fundamental limitations of linear MoE routing, namely routing in raw high-dimensional representation spaces and scale-sensitive dot-product scoring, which lead to routing ambiguity and insufficient expert specialization.
- We propose Low-rank & Lipschitz-controlled Routing (L2R), a unified routing framework that performs expert assignment in a low-rank latent routing space with Saturated Inner-Product Scoring (SIPS) and parameter-efficient multi-anchor routing, yielding smoother, more stable, and more expressive routing geometry.
- We validate L2R across both language and vision MoE settings, including large-scale language models and vision backbones on ImageNet, consistently improving routing stability, expert specialization, and overall performance.

## 2. Related Work

**Router Design in Sparse MoE.** Most modern sparse MoE systems still rely on raw-space linear routing, where expert logits are produced by a single linear projection in the backbone representation space, e.g., in OLMoE (Muenennighoff et al., 2025), Mixtral (Jiang et al., 2024), Qwen2-MoE (Yang et al., 2024), and DeepSeek-MoE (Dai et al., 2024), as well as vision MoE variants such as V-MoE (Riquelme et al., 2021), Mod-Squad (Chen et al., 2023), and ASE (Yang et al., 2025). Recent studies revisit router design from multiple angles: improving routing expressiveness (e.g., Router Upcycling (Ran et al., 2025) and attention-based routing in Yuan 2.0-M32 (Wu et al., 2024a)), and improving stability and utilization via auxiliary objectives and routing variants (Shazeer et al., 2017; Lepikhin et al., 2020; Fedus et al., 2022). Despite these advances, the routing score is still typically produced by *linear scoring in a high-dimensional space*, which leaves the scoring geometry sensitive to scale and high-dimensional concentration.

**Geometry-Aware Latent-Space Routing.** Another line of work performs routing in a *latent space* and adopts angle-aware similarities (Chi et al., 2022; Nguyen et al., 2025; Wu et al., 2024b). X-MoE (Chi et al., 2022) projects representations to a lower-dimensional space and uses cosine scoring to alleviate collapse in high-dimensional gating. Different from prior works, our study emphasizes two structural limitations that jointly weaken discriminability under raw-space routing: representation mismatch and angular concentration. We further observe that common rank heuristics (e.g., scaling rank with the number of experts) can still yield an angle-concentrated routing geometry in practice, motivating an ultra-low yet *consistent* rank across settings. Within this latent-space routing paradigm, L2R introduces *SIPS*, a Lipschitz-controlled scoring geometry that retains magni-

tude cues while explicitly bounding their effective influence (instead of discarding magnitude as cosine scoring), and improves expressiveness via lightweight multi-anchor heads.

### 3. Methodology

In this section, we first introduce the standard formulation of MoE architecture and the commonly adopted linear routing mechanism. We then present the proposed L2R framework that reshapes both the routing space and the scoring geometry for stable and expressive expert specialization.

#### 3.1. Preliminaries

**Mixture-of-Experts.** MoE models scale network capacity by replicating a sub-module, such as the feed-forward network (FFN) in a Transformer block, into a set of  $N$  parallel experts and activating only a sparse subset per input token (Cai et al., 2025). Given an input representation  $\mathbf{x} \in \mathbb{R}^d$ , a router  $g(\cdot)$  first produces routing logits:

$$\mathbf{z} = g(\mathbf{x}) \in \mathbb{R}^N, \quad (1)$$

where each element  $z_i$  reflects the affinity between the token and expert  $E_i$ . The logits are then normalized via a softmax function with temperature  $\tau$  to obtain routing scores:

$$\mathbf{s} = \text{Softmax}(\mathbf{z}/\tau) \in \mathbb{R}^N. \quad (2)$$

A sparse gating mechanism subsequently selects the top- $k$  experts, and the final MoE output is computed as:

$$\mathbf{y} = \mathbf{x} + \sum_{i \in \mathcal{T}} s_i E_i(\mathbf{x}), \quad \mathcal{T} = \text{TopK}(\mathbf{s}, k), \quad (3)$$

where  $\mathcal{T}$  denotes the indices of the selected experts. The routing scores jointly determine expert activation and their relative contributions, thereby defining the effective mixture geometry and influencing expert specialization (Dikkala et al., 2023).

**Linear Router.** In most existing MoE architectures (Muennighoff et al., 2025; Jiang et al., 2024; Yang et al., 2024; Dai et al., 2024), the router  $g(\cdot)$  is implemented as a dense linear transformation:

$$g(\mathbf{x}) = \mathbf{x} \mathbf{W}_g, \quad \mathbf{W}_g = [\mathbf{w}_1, \dots, \mathbf{w}_N] \in \mathbb{R}^{d \times N}, \quad (4)$$

where each column  $\mathbf{w}_i$  serves as the geometric anchor of expert  $E_i$ . The routing logit for expert  $E_i$  is computed as:

$$z_i = \mathbf{x}^\top \mathbf{w}_i, \quad (5)$$

which induces a partition of the high-dimensional representation space  $\mathbb{R}^d$  by linear decision hyperplanes defined by  $\{\mathbf{w}_i\}_{i=1}^N$ . This formulation performs expert assignment directly in raw backbone feature space using unbounded dot-product scoring, and thus inherits representation mismatch and scale-sensitive routing behaviors.

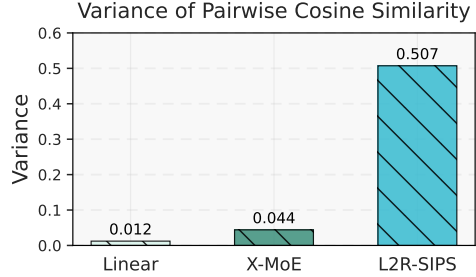


**Figure 2. Variance of pairwise cosine similarity in routing spaces.** We compare the layer-averaged variance of pairwise token cosine similarities in the latent routing space for Linear, X-MoE (Chi et al., 2022), and L2R-SIPS applied to OLMoE (Muennighoff et al., 2025). For L2R-SIPS, we use rank  $r=2$ , hence the isotropic reference corresponds to the 2D value (0.5). While Linear and X-MoE exhibit near-zero variance, L2R-SIPS attains a much higher variance, indicating substantially improved angular diversity.

#### 3.2. Low-Rank Routing

Linear routers perform expert assignment directly in the raw, high-dimensional backbone representation space. This design induces two structural limitations: 1) *representation mismatch* and 2) *high-dimensional concentration*, which fundamentally limit expert specialization.

**Representation Mismatch.** Backbone representations  $\mathbf{x}$  are primarily optimized for representation learning and downstream task prediction, rather than for expert discrimination. Consequently, the router is forced to operate in a *passive* feature space that is not explicitly shaped for separating tokens into expert-specific clusters. Especially in LLMs, semantic factors in such representations are often highly entangled due to superposition effects (Elhage et al., 2022), and token distributions are not encouraged to organize into well-separated expert-aware regions. This representation mismatch makes it difficult for a linear router to induce stable and semantically coherent expert assignments.

**High-Dimensional Concentration.** Linear routing typically operates in a high-dimensional regime with  $d \gg N$  (e.g.,  $d = 4,096$  with  $N \leq 64$ ) (Cai et al., 2025). In such spaces, angular similarities tend to concentrate (Cai et al., 2013), causing random or weakly structured vectors to become nearly orthogonal. Figure 2 provides direct empirical evidence of this phenomenon in OLMoE (Muennighoff et al., 2025): backbone token representations for Linear routers exhibit near-zero variance in pairwise cosine similarity, indicating a highly concentrated angular geometry. As a result, routing logits across experts have poorly separated margins, leading to ambiguous expert selection. Moreover, the large dimensionality of the routing space significantly enlarges the search space for expert anchors, making anchor optimization increasingly dependent on initialization and hindering effective expert positioning.

**Low-Rank Latent Routing Space.** To address the above limitations, we introduce a shared low-rank latent routing space that explicitly decouples routing from raw backbone geometry. Specifically, we parameterize routing through a shared projection:

$$\mathbf{q} = f(\mathbf{x}) = \mathbf{x} \mathbf{W}_q, \quad \mathbf{W}_q \in \mathbb{R}^{d \times r}, \quad r \ll d, \quad (6)$$

where  $\mathbf{q} \in \mathbb{R}^r$  denotes the routing-specific query representation. Each expert  $E_i$  is associated with a learnable anchor  $\mathbf{k}_i \in \mathbb{R}^r$  in this latent routing space, and routing logits are computed by matching  $\mathbf{q}$  with  $\{\mathbf{k}_i\}$ . This can be viewed as an attention-like operation, where  $\mathbf{q}$  serves as a routing query and  $\mathbf{k}_i$  as expert keys.

This formulation yields two immediate benefits: First, the shared projection  $\mathbf{W}_q$  explicitly learns a routing-oriented subspace, transforming backbone features into a space tailored for expert discrimination and mitigating raw-space representation mismatch. Second, routing in the compressed space  $\mathbb{R}^r$  substantially reduces geometric concentration (as presented in Figure 2) and the anchor search space, enabling more stable anchor positioning and more discriminative expert specialization.

### 3.3. Saturated Inner-Product Scoring (SIPS)

In this section, we analyze the limitations of standard dot-product scoring and introduce Saturated Inner-Product Scoring (SIPS), a bounded scoring geometry that balances the contributions of magnitude and angle for stable and expressive expert selection.

**Limitations of Dot-Product Scoring.** With low-rank routing (Section 3.2), a standard dot product typically computes logits as:

$$z_i = \mathbf{q}^\top \mathbf{k}_i = \|\mathbf{q}\| \|\mathbf{k}_i\| \cos \theta(\mathbf{q}, \mathbf{k}_i). \quad (7)$$

This coupling entangles *directional alignment* with *feature scale*. In practice, (i) token magnitudes  $\|\mathbf{q}\|$  can vary substantially (especially in LLMs, where certain token patterns yield unusually large activations), which scales all logits and effectively induces an input-dependent softmax temperature; and (ii) anchor norms  $\|\mathbf{k}_i\|$  modulate inter-expert logit gaps and can dominate the competition, since increasing  $\|\mathbf{k}_i\|$  often provides an easier route to raising scores than improving angular alignment. Together, these effects make routing scale-sensitive and encourage norm-dominated expert competition, introducing ambiguity in expert selection and weakening expert specialization.

**Geometric Visualization.** Figure 3 visualizes the logit landscape by fixing an expert anchor  $\mathbf{k}$  and sweeping query locations  $\mathbf{q}$  in a 2D routing plane. Under standard dot-product scoring (Figure 3a), level sets are nearly parallel

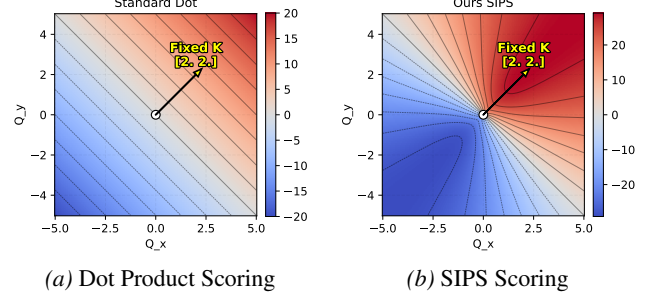


**Figure 3. Score landscapes under fixed expert anchor.** Heatmaps visualize routing logits as a function of query location  $\mathbf{q} = (Q_x, Q_y)$  with a fixed anchor  $\mathbf{k} = [2, 2]$ . Standard dot-product yields a linear half-space separation with unbounded magnitude effects, while SIPS reshapes the landscape into a bounded, angle-sensitive geometry that is more amenable to stable routing.

lines, and the score grows linearly with  $\|\mathbf{q}\|$ , hence a large region shares similar scores, yielding weak angular discrimination and making expert selection sensitive to magnitude variations. This motivates a bounded scoring geometry that sharpens directional preference while controlling radial score growth, which we formalize next as SIPS.

**SIPS: Rebalancing Scale and Angle.** Cosine-style scoring like X-MoE (Chi et al., 2022) stabilizes routing by removing magnitude factors, but it also discards a potentially informative signal for adaptive gating. In contrast, SIPS rebalances *scale* and *angle*: it preserves magnitude information for adaptive scoring, while explicitly bounding its influence so that routing remains stable and controllable. Concretely, SIPS factorizes each logit into a bounded magnitude term and an angular term:

$$z_i = \phi(\|\mathbf{q}\|) \psi(\|\mathbf{k}_i\|) \cos \theta_i, \quad \cos \theta_i = \frac{\mathbf{q}^\top \mathbf{k}_i}{\|\mathbf{q}\| \|\mathbf{k}_i\|}, \quad (8)$$

where  $\phi(\cdot)$  and  $\psi(\cdot)$  are nonnegative scalar transforms. Compared to the previous methods, SIPS bounds the scale sensitivity in both tokens and anchors, while preserving the semantic role of angles and retaining a controlled contribution from magnitudes.

**Query Magnitude Transform  $\phi(\|\mathbf{q}\|)$ .** We bound query magnitudes through a *normalize-then-saturate* design. Normalization is applied first to stabilize the distribution of query norms: for vision models, we apply BatchNorm to the scalar norm  $\|\mathbf{q}\|$ , while for LLMs we apply RMSNorm (Zhang & Sennrich, 2019) to the router input before the projection  $\mathbf{W}_q$ . We then define a bounded query magnitude transform:

$$\phi(\|\mathbf{q}\|) = \gamma \left( 1 + \beta \tanh(\widehat{\|\mathbf{q}\|}) \right), \quad (9)$$

where  $\widehat{\|\mathbf{q}\|}$  denotes the normalized query norm after the above normalization step. This yields a controllable interval:

$$\phi(\|\mathbf{q}\|) \in [\gamma(1 - \beta), \gamma(1 + \beta)]. \quad (10)$$

Here,  $\beta \in [0, 1]$  controls how much magnitude participates in expert selection ( $\beta = 0$  removes magnitude effects), and  $\gamma$  sets the overall logit scale (equivalently, it rescales logits and modulates the effective softmax temperature). This design mitigates excessively small logits for low-magnitude queries, while  $\tanh(\cdot)$  limits extreme magnitudes and prevents outliers from inducing overly sharp routing, hence improving routing stability.

We provide an additional 3D score-landscape comparison across dot-product, cosine, and SIPS with varying  $\beta$  in Appendix A, which further illustrates the near-origin smoothness and controlled radial growth induced by query-magnitude saturation.

**Anchor Magnitude Transform  $\psi(\|\mathbf{k}_i\|)$ .** Anchor norms regulate inter-expert contribution and competitiveness under top- $k$  aggregation and hence should not be fully removed. However, to prevent norm-dominated competition, we compress anchor magnitudes around 1:

$$\psi(\|\mathbf{k}_i\|) = 1 + \frac{\|\mathbf{k}_i\| - 1}{p}. \quad (11)$$

With larger  $p$ , the marginal logit gain from increasing  $\|\mathbf{k}_i\|$  is damped, encouraging experts to specialize primarily via angular alignment. We initialize anchors on the unit sphere ( $\|\mathbf{k}_i\| = 1$ ), so  $\psi(\|\mathbf{k}_i\|)$  is centered at 1 at initialization and deviations reflect learned competitiveness.

**Lipschitz-Controlled Score Geometry.** A key effect of SIPS is to *explicitly upper-bound the logit sensitivity* to scale variations, yielding a smoother and more controllable scoring geometry. Recall that in Equation (8),  $z_i = \phi(\|\mathbf{q}\|) \psi(\|\mathbf{k}_i\|) \cos \theta_i$ , the angular term satisfies  $\cos \theta_i \in [-1, 1]$  and is therefore intrinsically bounded. Consequently, scale-induced instability in dot-product scoring primarily arises from the magnitude factors  $\phi(\|\mathbf{q}\|)$  and  $\psi(\|\mathbf{k}_i\|)$ . SIPS addresses this by (i) bounding the query scale via  $\phi(\|\mathbf{q}\|)$  (Equation (9)) and (ii) compressing anchor norms around 1 via  $\psi(\|\mathbf{k}_i\|)$  (Equation (11)). These designs not only bound the attainable logit magnitude, but also bound the *slope* of  $z_i$  with respect to  $\|\mathbf{q}\|$  and  $\|\mathbf{k}_i\|$ , which directly translates into a smaller Lipschitz constant of the scoring map along the radial directions. Geometrically, this reshapes the fixed-anchor score field from an unbounded linear plane (Figure 3a) to a direction-selective landscape with controlled radial growth (Figure 3b), mitigating norm-driven ambiguity and improving the stability of expert selection. Formal gradient-sensitivity analysis and the resulting Lipschitz bounds for Equation (8) are provided in Appendix B.

### 3.4. Multi-Anchor Heads

While low-rank routing with SIPS provides a stable and discriminative scoring geometry, representing each expert with a single anchor can be restrictive when an expert needs to accommodate multiple semantic modes in the routing space. To increase routing expressiveness without introducing heavy routing overhead, we propose **multi-anchor heads**, which associate each expert with multiple anchors in the low-rank routing space.

**Multi-Anchor Parameterization.** For each expert  $E_i$ , we maintain  $H$  anchors  $\{\mathbf{k}_{i,h}\}_{h=1}^H$ , where  $\mathbf{k}_{i,h} \in \mathbb{R}^r$ . Given a routing query  $\mathbf{q}$ , we compute anchor-level logits under the SIPS geometry:

$$z_{i,h} = \phi(\|\mathbf{q}\|) \psi(\|\mathbf{k}_{i,h}\|) \cos \theta_{i,h}, \quad (12)$$

where  $\cos \theta_{i,h} = \frac{\mathbf{q}^\top \mathbf{k}_{i,h}}{\|\mathbf{q}\| \|\mathbf{k}_{i,h}\|}$ . We then aggregate  $\{z_{i,h}\}_{h=1}^H$  into an expert-level logit  $z_i$  via log-sum-exp (LSE) pooling (Jia et al., 2012):

$$z_i = \text{LSE}(\{z_{i,h}\}_{h=1}^H) = \log \sum_{h=1}^H \exp(z_{i,h}), \quad (13)$$

Compared to hard max pooling, LSE provides a smooth approximation that yields more stable gradients while still emphasizing the best-matching anchor. Routing then proceeds as in Section 3.1 by applying softmax and top- $k$  selection on  $\{z_i\}_{i=1}^N$ . Geometrically, multi-anchor heads allow each expert to represent a union of directional regions in the routing space, improving coverage of multi-view semantics.

Crucially, the bounded SIPS geometry (Section 3.3) makes these prototypes *trainable and composable*: logits are less dominated by scale, so anchors compete primarily through directional alignment rather than norm inflation, which stabilizes multi-prototype learning and encourages expert co-operation.

**Parameter Efficiency.** Multi-anchor heads only add low-dimensional anchors in  $\mathbb{R}^r$  and do not replicate the shared projection  $\mathbf{W}_q$ . As a result, the added parameters scale as  $O(NHr)$  and the extra computation is limited to low-rank inner products. A comprehensive efficiency analysis of L2R is provided in Appendix C.

**Initialization.** To align with the SIPS magnitude transforms, we initialize anchors on the unit sphere in  $\mathbb{R}^r$  (i.e.,  $\|\mathbf{k}_{i,h}\| = 1$ ) so that the initial competition is primarily driven by angular alignment, while norm-based competitiveness is learned gradually through  $\psi(\cdot)$ .

### 3.5. Optimization Objective

L2R is trained under the standard objective used in sparse MoE models, without introducing additional loss terms. The

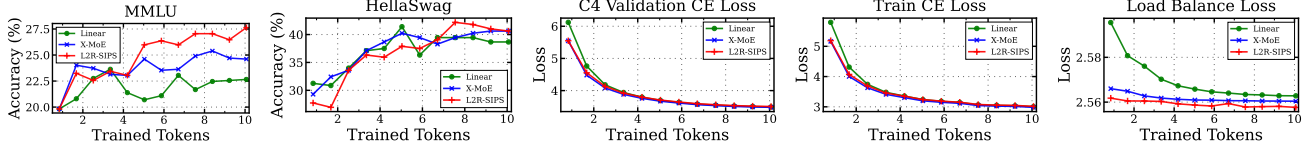


Figure 4. OLMoE training dynamics. Curves show MMLU and HellaSwag accuracies, C4 (Raffel et al., 2020) validation cross-entropy (CE), training CE, and load-balance loss. L2R exhibits clear convergence over 10B tokens and consistently improves MMLU/HellaSwag.

objective combines the task loss with auxiliary regularizers for routing stability and expert utilization:

$$\mathcal{L} = \mathcal{L}_{\text{task}} + \lambda_{\text{bal}} \mathcal{L}_{\text{bal}} + \lambda_z \mathcal{L}_z, \quad (14)$$

where  $\mathcal{L}_{\text{task}}$  is the task-specific training loss,  $\mathcal{L}_{\text{bal}}$  is the standard load-balancing loss (Fedus et al., 2022) that encourages uniform expert usage, and  $\mathcal{L}_z$  is the router z-loss (Zoph et al., 2022) for stabilizing routing logits during large-scale LLM training. The coefficients  $\lambda_{\text{bal}}$  and  $\lambda_z$  weight the auxiliary terms. Following OLMoE (Muennighoff et al., 2025), we apply  $\mathcal{L}_z$  for LLM experiments and omit it for vision experiments. Formal definitions of  $\mathcal{L}_{\text{bal}}$  and  $\mathcal{L}_z$  are provided in Appendix D.

## 4. Experiments

This section evaluates L2R on both language and vision MoE systems. We first study large-scale pretraining on OLMoE (Muennighoff et al., 2025) and report downstream benchmark performance under the OLMoE evaluation protocol. We then validate generality on a vision MoE system by training a ViT-S (Touvron et al., 2021) backbone on ImageNet-1K (Russakovsky et al., 2015).

### 4.1. LLM Experiments: OLMoE Pretraining

L2R is evaluated on OLMoE (Muennighoff et al., 2025), an open MoE language model suite. The backbone and training recipe follow the OLMoE reference configuration with  $N=64$  experts and top- $k=8$  sparse activation. All models are trained *from scratch* for 10B tokens on a distribution-matched subset of the official OLMoE pretraining mixture; subset construction and domain statistics are reported in Appendix E. Unless stated otherwise, L2R uses rank  $r=2$  and  $H=16$  multi-anchor heads. For SIPS, we use  $\gamma=1$ ,  $\beta=1$  for the query transform (Equation 9) and  $p=4$  for the anchor transform (Equation 11). Full hyperparameters and implementation details are provided in Appendix F.1. All runs are conducted on an  $8 \times$  NVIDIA B200 setup.

**Objective.** Training minimizes the standard cross entropy loss together with the auxiliary router regularizers adopted by OLMoE, including load-balancing loss and router z-loss (Section 3.5). Following OLMoE, the corresponding weights are set to  $\lambda_{\text{bal}}=0.01$  and  $\lambda_z=0.001$ .

**Compared Routers and L2R Variants.** The original OLMoE linear router is replaced by each of the compared routing designs. Baselines include the standard Linear router and a cosine scoring method X-MoE (Chi et al., 2022). L2R is evaluated under different scoring geometries, including L2R (Dot), L2R (Cosine), and the proposed L2R (SIPS).

**Downstream Evaluation Protocol.** We follow the downstream evaluation protocol and reporting conventions of OLMoE (Muennighoff et al., 2025). Specifically, we track a fixed set of lightweight commonsense and knowledge benchmarks (e.g., MMLU (Hendrycks et al., 2021), ARC-E (Clark et al., 2018), BoolQ (Clark et al., 2019), HellaSwag (Zellers et al., 2019), PIQA (Bisk et al., 2020), SciQ (Welbl et al., 2017)) and report Overall as the average score across tasks. This suite is intentionally lightweight for 10B-token training to probe *early-stage* commonsense and knowledge capabilities while remaining stable and reproducible. Details of task selection and metrics are provided in Appendix H.

#### 4.1.1. MAIN RESULTS

**Training Dynamics.** Figure 4 summarizes training behavior over 10B tokens. All routers show smooth and monotonic loss reduction, confirming stable convergence under the OLMoE recipe. Throughout training, L2R consistently attains higher MMLU accuracy and remains competitive on HellaSwag. For both C4 (Raffel et al., 2020) validation CE and training CE, L2R closely tracks the angle-sensitive baseline (X-MoE) and converges faster than the Linear router, supporting the benefit of stronger angular discrimination for optimization and generalization. Finally, in terms of load-balance loss, L2R achieves faster and lower convergence, indicating more balanced expert utilization and stable routing dynamics.

Table 1. Overall performance at 10B tokens. Best results are in **bold**, and second-best results are underlined.

Method	MMLU	ARC-E	BoolQ	HSwag	PIQA	SciQ	Overall
Linear	22.7	<b>47.7</b>	60.0	38.7	61.1	66.8	40.5
X-MoE	24.6	<u>46.9</u>	60.0	<u>40.6</u>	<b>64.5</b>	68.8	<u>42.1</u>
L2R (Dot)	24.4	43.4	59.2	39.5	60.5	64.8	40.6
L2R (Cosine)	<u>24.9</u>	42.2	<u>61.1</u>	<b>42.2</b>	60.0	<b>72.7</b>	42.0
<b>L2R (SIPS)</b>	<b>27.6</b>	43.8	<b>61.7</b>	<u>40.6</u>	<u>62.3</u>	<u>71.5</u>	<b>43.4</b>

**Overall Performance.** Table 1 reports downstream evaluation results at 10B tokens. L2R with the proposed SIPS

achieves the best overall score (43.4) and ranks first or second on most benchmarks. Notably, L2R yields a substantial gain on MMLU, improving from 22.7 (Linear) and 24.6 (X-MoE) to 27.6, indicating stronger early-stage knowledge recall and reasoning on lightweight probes. We also observe an exception on ARC-E, where L2R trails the Linear router; consistent with the head ablation in Table 3, the ARC-E drop becomes more pronounced as the number of heads increases, suggesting that the multi-anchor specialization pattern may require longer training to benefit ARC-style multiple-choice questions fully.

**Angle Discrimination vs. Scale Domination.** The results reveal a consistent split between (i) *angle-sensitive* routing and (ii) *unconstrained dot-product* routing. Angle-sensitive designs (X-MoE, L2R (Cosine), and L2R (SIPS)) substantially outperform Linear and L2R (Dot) in overall quality, and also exhibit faster cross-entropy reduction during training (Figure 4), underscoring the importance of angular discrimination for reliable routing. Meanwhile, pure cosine scoring eliminates magnitude cues, whereas SIPS retains them with bounded influence. This controlled rebalancing yields stronger overall performance over X-MoE and L2R (Cosine), supporting the role of *controlled* magnitude in expressive yet stable expert aggregation.

#### 4.1.2. ABLATIONS STUDY

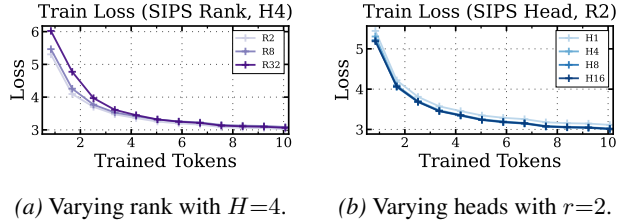


**Figure 5. Training dynamics (train cross-entropy loss) for ablations.** Both lower rank and more heads yield faster convergence over 10B tokens.

**Ablation on Routing Rank  $r$ .** Table 2 varies the routing rank with  $H=4$ . We find that ultra-low rank is sufficient:  $r=2$  achieves the best overall score, and larger ranks bring no consistent gains. Increasing  $r$  can reduce angular diversity (lower pairwise cosine-similarity variance in Figure 6), yielding a more concentrated routing geometry and less discriminative expert assignment. Consistently, Figure 5a shows slower training convergence for higher ranks. A similar trend is observed in our vision MoE study (Section 4.2).

**Table 2.** Ablation on Routing Rank  $r$  with  $H = 4$ .

Rank	MMLU	ARC-E	BoolQ	HSwag	PIQA	SciQ	Overall
2	25.2	<b>45.7</b>	62.1	<b>39.5</b>	61.1	69.1	<b>42.0</b>
8	23.2	43.4	<b>62.3</b>	38.3	<b>63.1</b>	68.8	41.0
32	<b>25.6</b>	43.4	59.4	39.1	61.1	<b>71.9</b>	41.9

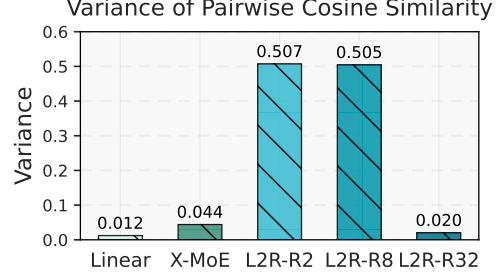


**Figure 6. Variance of pairwise cosine similarity in routing spaces.** We compare the layer-averaged variance of pairwise token cosine similarities in the routing space for Linear, X-MoE (Chi et al., 2022), and L2R-SIPS with different rank settings.

**Table 3.** Ablation on Multi-Anchor Heads ( $H$ ) with Rank  $r=2$ : Performance with router parameters. Router params over all MoE layers are reported with the percentage relative to the Linear router (2.097M) in parentheses.

$H$	Router Params	MMLU	ARC-E	BoolQ	HSwag	PIQA	SciQ	Overall
1	100.4K (4.79%)	25.5	<b>46.9</b>	60.0	37.5	60.5	69.9	41.9
4	106.5K (5.08%)	25.2	45.7	62.1	39.5	61.1	69.1	42.0
8	114.7K (5.47%)	25.2	45.3	60.2	39.8	<b>64.3</b>	68.4	42.1
16	131.1K (6.25%)	<b>27.6</b>	43.8	<b>61.7</b>	<b>40.6</b>	62.3	<b>71.5</b>	<b>43.4</b>

**Ablation on Multi-Anchor Heads  $H$ .** Table 3 varies the head count with  $r=2$ . Increasing  $H$  monotonically improves Overall performance, peaking at  $H=16$ , while incurring only a small router overhead (6.25% of the Linear router). This supports our motivation that multi-anchor heads increase routing expressiveness by allowing each expert to cover multiple modes in the low-rank space at negligible cost. Moreover, Figure 5b indicates faster training convergence with larger  $H$ . We also observe a consistent drop on ARC-E as  $H$  increases (aligning with Table 1), suggesting that this multi-mode specialization pattern may require longer training to fully realize ARC-E gains.

#### 4.1.3. ROUTING GEOMETRY AND EXPERT USAGE VISUALIZATIONS

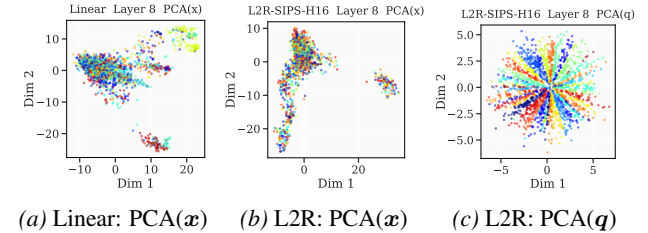


**Figure 7. Representation-space visualization at a middle layer (Layer 8).** PCA projections of token representations in the raw backbone space ( $x$ ) and the low-rank routing space ( $q$ ). Points are colored by the top-1 routed expert.

**Routing-Space Geometry.** Figure 7 contrasts token geometry in the raw backbone space  $x$  and the projected routing space  $q$ . Under Linear routing (Figure 7a), tokens concentrate in an anisotropic and “narrow” region, consistent

with the severe angular concentration quantified in Figure 6. In contrast, L2R learns a routing-oriented low-rank space where token directions are markedly more separable and form structured regions when stratified by top-1 expert assignments (Figure 7c). Tracing these same tokens back to the raw  $x$  space reveals wide dispersion (Figure 7b), which is consistent with a multi-anchor specialization pattern that each expert covers multiple semantic modes instead of a single compact cluster in  $x$ .

**Near-Origin Stability with SIPS.** Both the raw and projected routing spaces contain low-magnitude tokens around the origin, where routing is inherently noise-sensitive (cosine-style scoring can be particularly brittle to small angular perturbations). SIPS stabilizes this regime by imposing a bounded and smooth magnitude response, avoiding vanishing scores for low-norm queries, thereby improving stability without discarding magnitude information. Further diagnostics and ablations on  $\phi(\cdot)$  are provided in Appendix A.

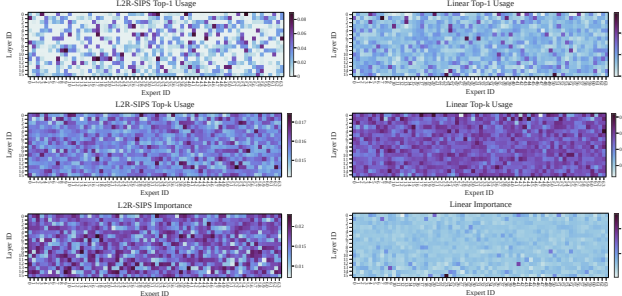


**Figure 8. Expert-usage patterns across layers.** From top to bottom: top-1 routing frequency, top- $k$  routing frequency, and importance-based routing weights. Each row is a Transformer layer, and each column is an expert.

**Expert Usage and Cooperation.** Figure 8 summarizes routing patterns across layers. Compared to Linear routing, L2R yields a sharper and more structured top-1 map, indicating clearer expert specialization, while maintaining broadly distributed top- $k$  usage, reflecting sustained cooperation under sparse activation. Importantly, regions with high top-1 frequency do not consistently align with peaks in the top- $k$  and importance maps, suggesting that L2R avoids single-expert domination and instead modulates multi-expert contributions via SIPS-controlled magnitude.

#### 4.2. Experiments with ViT on ImageNet

We further evaluate L2R on a vision MoE system by training a ViT-S (Touvron et al., 2021) backbone on ImageNet-1K (Russakovsky et al., 2015) from scratch for 300 epochs. We follow a standard ViT-S recipe with batch size 512 and apply MoE to the last 4 Transformer blocks. Unless stated otherwise, we use  $N=16$  experts with top- $k=2$  sparse activation, and train with only the load-balancing auxiliary loss

( $\lambda_{\text{bal}}=0.01$ ). For L2R, we set rank  $r=2$  and multi-anchor heads  $H=4$ , and reuse the same SIPS hyperparameters as in the LLM setting ( $\gamma=1$ ,  $\beta=1$ ,  $p=4$ ). All runs are conducted on  $4 \times$  A100 GPUs. Detailed configurations are summarized in Appendix F.2.

**Table 4.** Top-1 and Top-5 accuracy on ImageNet-1K with ViT-S backbone. Higher is better ( $\uparrow$ ).

Method	Top-1 (%) $\uparrow$	Top-5 (%) $\uparrow$
Linear	74.12	90.38
X-MoE	74.07	90.23
L2R (Dot)	74.96	91.23
L2R (Cosine)	75.32	91.36
<b>L2R (SIPS)</b>	<b>76.58</b>	<b>91.50</b>

**Performance on ImageNet.** Table 4 reports ImageNet results. L2R achieves the best performance, confirming that L2R with the proposed SIPS transfers effectively to vision MoE training. Notably, X-MoE (Chi et al., 2022) slightly underperforms the Linear router in this setting, whereas L2R variants yield consistent gains, suggesting that improving routing geometry is beneficial beyond the language domain.

**Table 5.** Ablation on Routing Rank  $r$  with  $H=4$ .

Rank	Top-1 (%) $\uparrow$	Top-5 (%) $\uparrow$
2	<b>76.58</b>	<b>91.50</b>
8	75.44	90.95
32	74.90	90.12

**Ablation on Routing Rank  $r$ .** Table 5 varies the routing rank with fixed  $H=4$ . Consistent with the LLM results, we find that ultra-low rank is sufficient:  $r=2$  performs best, while increasing rank to 8 or 32 degrades accuracy. This supports the same geometric conclusion that enlarging the routing space can reintroduce concentration effects and reduce angular separability, weakening expert discrimination even in vision settings.

## 5. Conclusion

We introduced **Low-rank & Lipschitz-controlled Routing (L2R)**, a routing framework that improves MoE specialization by jointly redesigning the routing space and scoring geometry. L2R replaces high-dimensional linear routing with a shared low-rank latent space, adopts Saturated Inner-Product Scoring (**SIPS**) to bound magnitude sensitivity while preserving controlled magnitude for adaptive expert weighting, and extends expressiveness with lightweight multi-anchor heads. Experiments on OLMoE pretraining and ViT-based ImageNet training show consistent gains, faster convergence, and balanced expert usage, indicating that L2R provides a practical and stable routing recipe across both language and vision MoE systems.

## Impact Statement

This work proposes a routing framework for Mixture-of-Experts models that improves routing stability, expert specialization, and efficiency through low-rank representations and Lipschitz-controlled scoring. By enabling more reliable sparse activation, the method can support more stable training and effective use of model capacity in large-scale language and vision models. The contribution is primarily technical and focuses on internal optimization of Mixture-of-Experts architectures, without introducing new application-level capabilities beyond existing scalable model designs; any broader societal impacts depend on downstream deployment choices.

## Acknowledgment

This research was supported in part by AMED Grant Number JP256f0137006, and JSPS KAKENHI Grant Numbers JP23K11141, JP23K21676, JP24K02942, JP24K23849, and JP25K21218.

## References

Bisk, Y., Zellers, R., Gao, J., Choi, Y., et al. Piqa: Reasoning about physical commonsense in natural language. In *Proc. AAAI*, volume 34, pp. 7432–7439, 2020.

Cai, T., Fan, J., and Jiang, T. Distributions of angles in random packing on spheres. *J. Mach. Learn. Res.*, 14(1):1837–1864, 2013.

Cai, W., Jiang, J., Wang, F., Tang, J., Kim, S., and Huang, J. A survey on mixture of experts in large language models. *IEEE Trans. Knowl. Data Eng.*, 2025.

Chen, Z., Shen, Y., Ding, M., Chen, Z., Zhao, H., Learned-Miller, E. G., and Gan, C. Mod-squad: Designing mixtures of experts as modular multi-task learners. In *Proc. CVPR*, pp. 11828–11837, 2023.

Chi, Z., Dong, L., Huang, S., Dai, D., Ma, S., Patra, B., Singhal, S., Bajaj, P., Song, X., Mao, X.-L., et al. On the representation collapse of sparse mixture of experts. In *Proc. NeurIPS*, pp. 34600–34613, 2022.

Clark, C., Lee, K., Chang, M.-W., Kwiatkowski, T., Collins, M., and Toutanova, K. Boolq: Exploring the surprising difficulty of natural yes/no questions. *arXiv preprint arXiv:1905.10044*, 2019.

Clark, P., Cowhey, I., Etzioni, O., Khot, T., Sabharwal, A., Schoenick, C., and Tafjord, O. Think you have solved question answering? try arc, the ai2 reasoning challenge. *arXiv preprint arXiv:1803.05457*, 2018.

Dai, D., Deng, C., Zhao, C., Xu, R., Gao, H., Chen, D., Li, J., Zeng, W., Yu, X., Wu, Y., et al. Deepseekmoe: Towards ultimate expert specialization in mixture-of-experts language models. *arXiv preprint arXiv:2401.06066*, 2024.

Dikkala, N., Ghosh, N., Meka, R., Panigrahy, R., Vyas, N., and Wang, X. On the benefits of learning to route in mixture-of-experts models. In *Proc. EMNLP*, pp. 9376–9396, 2023.

Elhage, N., Hume, T., Olsson, C., Schiefer, N., Henighan, T., Kravec, S., Hatfield-Dodds, Z., Lasenby, R., Drain, D., Chen, C., et al. Toy models of superposition. *arXiv preprint arXiv:2209.10652*, 2022.

Fedus, W., Zoph, B., and Shazeer, N. Switch transformers: Scaling to trillion parameter models with simple and efficient sparsity. *J. Mach. Learn. Res.*, 23(120):1–39, 2022.

Gale, T., Narayanan, D., Young, C., and Zaharia, M. Megablocks: Efficient sparse training with mixture-of-experts. In *Proc. MLSys*, volume 5, pp. 288–304, 2023.

Gu, Y., Tafjord, O., Kuehl, B., Haddad, D., Dodge, J., and Hajishirzi, H. OLMES: A standard for language model evaluations. In *Proc. NAACL*, pp. 5005–5033, 2025.

Hendrycks, D., Burns, C., Basart, S., Zou, A., Mazeika, M., Song, D., and Steinhardt, J. Measuring massive multitask language understanding. In *Proc. ICLR*, 2021.

Hwang, C., Cui, W., Xiong, Y., Yang, Z., Liu, Z., Hu, H., Wang, Z., Salas, R., Jose, J., Ram, P., et al. Tutel: Adaptive mixture-of-experts at scale. In *Proc. MLSys*, volume 5, pp. 269–287, 2023.

Jia, Y., Huang, C., and Darrell, T. Beyond spatial pyramids: Receptive field learning for pooled image features. In *Proc. CVPR*, pp. 3370–3377, 2012.

Jiang, A. Q., Sablayrolles, A., Roux, A., Mensch, A., Savary, B., Bamford, C., Chaplot, D. S., Casas, D. d. l., Hanna, E. B., Bressand, F., et al. Mixtral of experts. *arXiv preprint arXiv:2401.04088*, 2024.

Lepikhin, D., Lee, H., Xu, Y., Chen, D., Firat, O., Huang, Y., Krikun, M., Shazeer, N., and Chen, Z. Gshard: Scaling giant models with conditional computation and automatic sharding. *arXiv preprint arXiv:2006.16668*, 2020.

Muennighoff, N., Soldaini, L., Groeneveld, D., Lo, K., Morrison, J., Min, S., Shi, W., Walsh, P., Tafjord, O., Lambert, N., et al. OLMoE: Open mixture-of-experts language models. In *Proc. ICLR*, 2025.

Nguyen, H., Akbarian, P., Pham, T., Nguyen, T., Zhang, S., and Ho, N. Statistical advantages of perturbing cosine router in mixture of experts. In *Proc. ICLR*, 2025.

Raffel, C., Shazeer, N., Roberts, A., Lee, K., Narang, S., Matena, M., Zhou, Y., Li, W., and Liu, P. J. Exploring the limits of transfer learning with a unified text-to-text transformer. *J. Mach. Learn. Res.*, 21(140):1–67, 2020.

Ran, J., Zhao, G., Wu, Y., Zhu, D., Wu, L., Zhao, Y., Yang, T., Sun, L., Zhang, X., and Li, S. Router upcycling: Leveraging mixture-of-routers in mixture-of-experts upcycling. *arXiv preprint arXiv:2509.00679*, 2025.

Riquelme, C., Puigcerver, J., Mustafa, B., Neumann, M., Jenatton, R., Susano Pinto, A., Keysers, D., and Houlsby, N. Scaling vision with sparse mixture of experts. In *Proc. NeurIPS*, pp. 8583–8595, 2021.

Russakovsky, O., Deng, J., Su, H., Krause, J., Satheesh, S., Ma, S., Huang, Z., Karpathy, A., Khosla, A., Bernstein, M., et al. Imagenet large scale visual recognition challenge. *Int. J. Comput. Vis.*, 115(3):211–252, 2015.

Sakaguchi, K., Le Bras, R., Bhagavatula, C., and Choi, Y. Winogrande: An adversarial winograd schema challenge at scale. In *Proc. AAAI*, volume 34, pp. 8732–8740, 2020.

Shazeer, N., Mirhoseini, A., Maziarz, K., Davis, A., Le, Q., Hinton, G., and Dean, J. Outrageously large neural networks: The sparsely-gated mixture-of-experts layer. *arXiv preprint arXiv:1701.06538*, 2017.

Touvron, H., Cord, M., Douze, M., Massa, F., Sablayrolles, A., and Jégou, H. Training data-efficient image transformers & distillation through attention. In *Proc. ICML*, pp. 10347–10357, 2021.

Welbl, J., Liu, N. F., and Gardner, M. Crowdsourcing multiple choice science questions. *arXiv preprint arXiv:1707.06209*, 2017.

Wu, S., Luo, J., Chen, X., Li, L., Zhao, X., Yu, T., Wang, C., Wang, Y., Wang, F., Qiao, W., et al. Yuan 2.0-m32: Mixture of experts with attention router. *arXiv preprint arXiv:2405.17976*, 2024a.

Wu, X., Huang, S., Wang, W., Ma, S., Dong, L., and Wei, F. Multi-head mixture-of-experts. In *Proc. NeurIPS*, pp. 94073–94096, 2024b.

Yang, A., Yang, B., Hui, B., et al. Qwen2 technical report. *arXiv preprint arXiv:2407.10671*, 2024.

Yang, M., Togo, R., Li, G., Ogawa, T., and Haseyama, M. Adaptive shared experts with LoRA-based mixture of experts for multi-task learning. *arXiv preprint arXiv:2510.00570*, 2025.

Zellers, R., Holtzman, A., Bisk, Y., Farhadi, A., and Choi, Y. Hellaswag: Can a machine really finish your sentence? *arXiv preprint arXiv:1905.07830*, 2019.

Zhang, B. and Sennrich, R. Root mean square layer normalization. In *Proc. NeurIPS*, 2019.

Zoph, B., Bello, I., Kumar, S., Du, N., Huang, Y., Dean, J., Shazeer, N., and Fedus, W. St-moe: Designing stable and transferable sparse expert models. *arXiv preprint arXiv:2202.08906*, 2022.

## A. Additional Geometry of Query-Magnitude Saturation

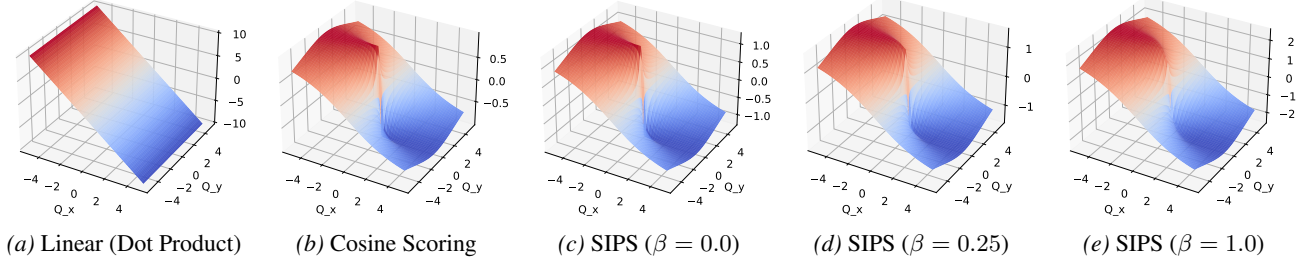


**Figure 9. Effect of query-magnitude saturation strength ( $\beta$ ) under a fixed anchor.** We fix the expert anchor at  $\mathbf{k} = [-2, 0]$  and visualize routing logits over query locations  $\mathbf{q} = (Q_x, Q_y)$  in a 2D routing plane (rank  $r = 2$ ). Dot-product scoring produces an unbounded, nearly half-space-like field dominated by radial growth (a), whereas cosine scoring removes magnitude effects entirely (b). SIPS interpolates between these extremes by preserving magnitude as a bounded confidence signal: increasing  $\beta$  enlarges the effective dynamic range of the bounded magnitude term while maintaining controlled radial growth (c–e).

Figure 9 provides a complementary 3D visualization of routing score landscapes under a fixed anchor, highlighting how different scoring rules respond to variations in query magnitude. We fix  $\mathbf{k} = [-2, 0]$  and sweep  $\mathbf{q} = (Q_x, Q_y)$  over a 2D routing plane, plotting the resulting logit value  $z(\mathbf{q}, \mathbf{k})$ .

**Dot-Product Scoring.** As shown in Figure 9a, standard dot-product scoring yields an (approximately) half-space-like field whose value grows linearly with  $\|\mathbf{q}\|$  along the radial direction. This implies that scale variations can dominate the score landscape, creating large regions with weak angular contrast while simultaneously allowing extreme magnitudes to induce overly sharp routing.

**Cosine Scoring.** Cosine scoring (Figure 9b) eliminates magnitude effects by normalizing both  $\mathbf{q}$  and  $\mathbf{k}$ , thereby improving global scale stability. However, the normalization introduces a sharp behavior around  $\|\mathbf{q}\| \approx 0$ , where small perturbations of low-norm queries can cause disproportionately large changes in direction (and thus in  $\cos \theta$ ). Since low-norm queries are also more susceptible to noise, this “origin sharpness” can translate into unstable and noisy expert selection.

**SIPS Scoring.** SIPS introduces a bounded query-magnitude transform  $\phi(\|\mathbf{q}\|) = \gamma(1 + \beta \tanh(\widehat{\|\mathbf{q}\|}))$  and thus treats magnitude as a *bounded confidence* factor rather than an unbounded amplifier. When  $\beta = 0$  (Figure 9c),  $\phi(\|\mathbf{q}\|)$  becomes a constant, and the logit reduces to a cosine-like form up to a global rescaling, removing magnitude participation. As  $\beta$  increases (Figure 9d and 9e), magnitude information is gradually reintroduced, but its influence remains strictly bounded; importantly, the score landscape becomes noticeably **smoother around the origin** while preserving **clear directional selectivity**. This yields a controlled radial growth together with improved near-origin smoothness, which empirically corresponds to more stable routing dynamics and less noise-sensitive expert selection.

**Takeaway.** Overall, Figure 9 illustrates that SIPS is not merely “bounded” in value, but also reshapes the score geometry into a smoother, angle-sensitive landscape. The saturation strength  $\beta$  governs how strongly query magnitude participates in routing: smaller  $\beta$  emphasizes angular discrimination with minimal scale effects, while larger  $\beta$  leverages magnitude as a bounded confidence signal without recovering the unbounded norm dominance of dot-product scoring.

## B. Gradient Sensitivity and Lipschitz Bounds of SIPS

We analyze the gradient sensitivity of the SIPS logit in Equation (8) and derive Lipschitz bounds under mild domain assumptions that match practical routing implementations.

**Setup.** For a single expert, define  $\rho = \|\mathbf{q}\|$ ,  $\kappa = \|\mathbf{k}\|$ ,  $\mathbf{u} = \mathbf{q}/\rho$ ,  $\mathbf{v} = \mathbf{k}/\kappa$ , and  $c = \mathbf{u}^\top \mathbf{v} = \cos \theta \in [-1, 1]$ . The SIPS logit can be written as:

$$z(\mathbf{q}, \mathbf{k}) = \phi(\rho) \psi(\kappa) c. \quad (15)$$

As in practice, we assume numerical stabilization by enforcing:

$$\rho \geq \varepsilon_q, \quad \kappa \geq \varepsilon_k, \quad (16)$$

for small  $\varepsilon_q, \varepsilon_k > 0$ .

**Cosine gradient bound.** Using  $\mathbf{u} = \mathbf{q}/\rho$  and treating  $\mathbf{v}$  as fixed, the cosine alignment satisfies:

$$\nabla_{\mathbf{q}} c = \frac{1}{\rho} (\mathbf{I} - \mathbf{u}\mathbf{u}^\top) \mathbf{v}, \quad \|\nabla_{\mathbf{q}} c\| \leq \frac{1}{\rho}. \quad (17)$$

Symmetrically:

$$\nabla_{\mathbf{k}} c = \frac{1}{\kappa} (\mathbf{I} - \mathbf{v}\mathbf{v}^\top) \mathbf{u}, \quad \|\nabla_{\mathbf{k}} c\| \leq \frac{1}{\kappa}. \quad (18)$$

**Gradient sensitivity of SIPS.** Differentiating Equation (15) yields:

$$\nabla_{\mathbf{q}} z = \psi(\kappa) \left( \phi'(\rho) c \mathbf{u} + \phi(\rho) \nabla_{\mathbf{q}} c \right), \quad (19)$$

$$\nabla_{\mathbf{k}} z = \phi(\rho) \left( \psi'(\kappa) c \mathbf{v} + \psi(\kappa) \nabla_{\mathbf{k}} c \right). \quad (20)$$

Using  $|c| \leq 1$  and Equations (17)–(18), we obtain:

$$\|\nabla_{\mathbf{q}} z\| \leq \psi(\kappa) \left( |\phi'(\rho)| + \frac{\phi(\rho)}{\rho} \right), \quad (21)$$

$$\|\nabla_{\mathbf{k}} z\| \leq \phi(\rho) \left( |\psi'(\kappa)| + \frac{\psi(\kappa)}{\kappa} \right). \quad (22)$$

**Lipschitz bounds on a practical domain.** A global Lipschitz constant requires bounded magnitudes. We therefore analyze  $z$  on the domain:

$$\mathcal{D} = \{(\mathbf{q}, \mathbf{k}) : \rho \in [\varepsilon_q, \rho_{\max}], \kappa \in [\varepsilon_k, \kappa_{\max}]\}, \quad (23)$$

where  $\rho_{\max}$  is induced by normalization and  $\kappa_{\max}$  is induced by weight decay or explicit norm control. Assume on  $\mathcal{D}$  that  $\phi(\rho) \leq \phi_{\max}$ ,  $|\phi'(\rho)| \leq L_\phi$ , and  $\psi(\kappa) \leq \psi_{\max}$ ,  $|\psi'(\kappa)| \leq L_\psi$ . Then by Equations (21)–(22),  $z$  is Lipschitz in  $\mathbf{q}$  and  $\mathbf{k}$  with:

$$\text{Lip}_{\mathbf{q}}(z) \leq \psi_{\max} \left( L_\phi + \frac{\phi_{\max}}{\varepsilon_q} \right), \quad (24)$$

$$\text{Lip}_{\mathbf{k}}(z) \leq \phi_{\max} \left( L_\psi + \frac{\psi_{\max}}{\varepsilon_k} \right). \quad (25)$$

A joint Lipschitz bound with respect to  $(\mathbf{q}, \mathbf{k})$  follows by combining the two gradient bounds.

**Instantiation for our transforms.** For the query transform  $\phi(\rho) = \gamma(1 + \beta \tanh(\hat{\rho}))$ , we have:

$$\phi_{\max} = \gamma(1 + \beta), \quad \left| \frac{d\phi}{d\hat{\rho}} \right| \leq \gamma\beta. \quad (26)$$

Thus  $L_\phi \leq \gamma\beta L_{\text{norm}}$  if the scalar normalization map  $\rho \mapsto \hat{\rho}$  is  $L_{\text{norm}}$ -Lipschitz on  $\mathcal{D}$ . For the anchor transform  $\psi(\kappa) = 1 + (\kappa - 1)/p$ , we have:

$$L_\psi = \frac{1}{p}, \quad \psi_{\max} = 1 + \frac{\kappa_{\max} - 1}{p} \text{ on } \mathcal{D}. \quad (27)$$

**Contrast to dot-product scoring.** For  $z_{\text{dot}}(\mathbf{q}, \mathbf{k}) = \mathbf{q}^\top \mathbf{k}$ , the gradients are  $\nabla_{\mathbf{q}} z_{\text{dot}} = \mathbf{k}$  and  $\nabla_{\mathbf{k}} z_{\text{dot}} = \mathbf{q}$ , so sensitivity grows linearly with  $\|\mathbf{k}\|$  and  $\|\mathbf{q}\|$ . In contrast, SIPS bounds the radial sensitivity via bounded/contractive magnitude transforms, and therefore yields an explicit mechanism to control the Lipschitz behavior of the scoring map.

## C. Complexity and Efficiency

We analyze the routing overhead of L2R and compare it to the standard linear router. Let  $d$  be the backbone hidden dimension,  $N$  the number of experts,  $r$  the routing rank ( $r \ll d$ ),  $k$  the top- $k$  sparsity, and  $H$  the number of anchors per expert in multi-anchor heads.

**Baseline: Linear Routing.** A standard linear router computes logits by  $z = xW_g$  with  $W_g \in \mathbb{R}^{d \times N}$  as Equation (4). The routing parameter count is:

$$P_{\text{lin}} = dN, \quad (28)$$

and the per-token routing cost is dominated by the matrix-vector product:

$$C_{\text{lin}} \approx O(dN). \quad (29)$$

**L2R Routing.** L2R replaces the high-dimensional projection by (i) a shared low-rank projection  $W_q \in \mathbb{R}^{d \times r}$  and (ii) expert anchors  $\{k_{i,h}\}$  in  $\mathbb{R}^r$ . With multi-anchor heads, L2R maintains  $NH$  anchors.

**Parameters.** The routing parameters consist of  $W_q$  and anchors:

$$P_{\text{L2R}} = dr + NHr. \quad (30)$$

Thus, the parameter reduction over linear routing is:

$$\frac{P_{\text{L2R}}}{P_{\text{lin}}} = \frac{dr + NHr}{dN} = \frac{r}{N} + \frac{Hr}{d}. \quad (31)$$

In typical MoE settings where  $d \gg r$  and  $N$  is moderate-to-large, the router overhead is substantially reduced, and the multi-anchor term remains small because it scales only with  $r$ .

**Computation.** L2R first computes  $q = xW_q$  with cost  $O(dr)$ , then evaluates anchor logits by low-rank inner products with cost  $O(NHr)$ :

$$C_{\text{L2R}} \approx O(dr + NHr). \quad (32)$$

SIPS adds only lightweight scalar transforms on norms and does not change the asymptotic complexity. Multi-anchor pooling aggregates  $H$  logits per expert as Equation (13), which is  $O(NH)$  and negligible compared to  $O(NHr)$  when  $r \geq 2$ .

**Measured Router Parameters on OLMoE.** Table 6 reports router parameter counts under different rank–head combinations on OLMoE (16 MoE layers,  $d=2048$ ,  $N=64$ ). Each entry shows the total router parameters aggregated over all MoE layers, followed by the percentage relative to the Linear router (2.097M parameters). Across all tested configurations, router parameters remain negligible compared to the full model size ( $\sim 6.92\text{B}$ ), and multi-anchor heads incur only a minor additional cost.

**Table 6. Router parameters under different rank  $r$  and head  $H$  settings on OLMoE.** Each cell reports total router params over all MoE layers, with the percentage relative to the Linear router (2.097M) in parentheses.

Rank $r \setminus$ Heads $H$	1	2	4	8	16
2	100.352K (4.79%)	102.400K (4.88%)	106.496K (5.08%)	114.688K (5.47%)	131.072K (6.25%)
4	167.936K (8.01%)	172.032K (8.20%)	180.224K (8.59%)	196.608K (9.38%)	229.376K (10.94%)
8	303.104K (14.46%)	311.296K (14.84%)	327.680K (15.62%)	360.448K (17.19%)	425.984K (20.32%)
16	573.440K (27.34%)	589.824K (28.12%)	622.592K (29.69%)	688.128K (32.81%)	819.200K (39.07%)
32	1.114M (53.11%)	1.147M (54.68%)	1.212M (57.81%)	1.343M (64.06%)	1.606M (76.59%)

**Discussion: FLOPs vs. Wall-Clock Time.** Although  $O(dr + NHr)$  can be significantly smaller than  $O(dN)$ , practical end-to-end speedups are not guaranteed. Routing is often not the dominant cost of MoE blocks, and the L2R router introduces additional element-wise operations (normalization, tanh, and pooling) that may be less hardware-efficient than a single dense GEMM.

## D. Optimization Objective Details

We train L2R under the standard optimization objective adopted by prior sparse MoE models, without introducing additional loss terms. Specifically, the objective consists of the task loss, a load-balancing loss to encourage uniform expert utilization, and the router z-loss (Zoph et al., 2022) used in OLMoE (Muennighoff et al., 2025) to stabilize gating logits in large-scale language model training.

**Load-Balancing Loss.** Following prior MoE work, we employ a load-balancing loss to prevent expert under-utilization and collapse. Let  $s_{t,i}$  denote the routing probability assigned to expert  $i$  for token  $t$ , and let  $\mathbb{I}[i \in \mathcal{T}_t]$  indicate whether expert  $i$  is selected in the top- $k$  routing set for token  $t$ . Over a batch of  $T$  tokens, we define the average routing probability and empirical expert usage as:

$$\bar{s}_i = \frac{1}{T} \sum_{t=1}^T s_{t,i}, \quad f_i = \frac{1}{T} \sum_{t=1}^T \mathbb{I}[i \in \mathcal{T}_t]. \quad (33)$$

The load-balancing loss is then given by:

$$\mathcal{L}_{\text{bal}} = N \sum_{i=1}^N \bar{s}_i f_i, \quad (34)$$

which encourages alignment between routing probabilities and actual expert assignments.

**Z-Loss.** Following OLMoE (Muennighoff et al., 2025), we additionally employ the router z-loss for large-scale language model training to regularize the magnitude of pre-softmax routing logits. Let  $\mathbf{z}_t \in \mathbb{R}^N$  denote the routing logits for token  $t$ . The z-loss is defined as:

$$\mathcal{L}_z = \frac{1}{T} \sum_{t=1}^T \left( \log \sum_{i=1}^N \exp(z_{t,i}) \right)^2, \quad (35)$$

which discourages excessively large logits and improves training stability. We apply this term only in LLM training, and omit it for vision and multi-task learning experiments.

**Overall Objective.** The final optimization objective is:

$$\mathcal{L} = \mathcal{L}_{\text{task}} + \lambda_{\text{bal}} \mathcal{L}_{\text{bal}} + \lambda_z \mathcal{L}_z, \quad (36)$$

where  $\lambda_{\text{bal}}$  and  $\lambda_z$  control the relative weights of the auxiliary losses.

## E. Experiments with OLMoE: Data Preparation

*Table 7. Distribution-matched 200B subset of allenai/OLMoE-mix-0924.* We randomly sample complete shards per domain with a fixed seed (2025) to obtain a  $\approx$ 200B-token subset while preserving the domain mixture ratios of the full dataset.

Domain	Total shards	Selected shards	Approx. tokens (B)	Token share (%)
dclm	1970	97	190.06	94.01
starcoder	863	43	5.03	2.49
pes2o	26	1	2.20	1.09
open-web-math	26	1	0.49	0.24
algebraic-stack	16	1	0.79	0.39
wiki	2	1	1.84	0.91
<b>Total</b>	2903	144	200.41	100.00

**Source dataset.** We use the official OLMoE pretraining mixture `allenai/OLMoE-mix-0924`, which contains approximately 4.07T tokens spanning six domains. To accelerate experimentation while preserving the training distribution, we construct a smaller, distribution-matched subset by sampling complete shards from each domain in proportion to its scale in the full mix.

**Distribution-matched shard sampling.** Let  $\mathcal{D} = \{d\}$  denote the set of domains and let  $S_d$  be the number of shards in domain  $d$ . Given a target budget of  $T$  tokens (e.g.,  $T = 200B$ ), we randomly sample a fixed number of shards from each domain using a fixed seed (seed=2025), such that the resulting token mass closely matches the original mixture proportions. Concretely, we sample shards without replacement within each domain, and keep the domain-wise sampling ratios aligned with the full dataset scale. Table 7 reports the resulting domain composition for the 200B subset used in our main OLMoE experiments.

**Multiple subset sizes.** Using the same procedure, we also generate additional subsets at smaller scales (10B/50B/100B tokens) for fast ablations and debugging. All subsets are constructed by the same distribution-matched shard sampling strategy to ensure comparability across scales.

## F. Training Configuration Details

### F.1. Training Configuration for OLMoE Experiments

This appendix reports the core training hyperparameters for OLMoE experiments in Table 8. To isolate routing effects, we follow the original OLMoE (Muennighoff et al., 2025) settings and keep the backbone architecture, optimization recipe, and MoE auxiliary losses fixed across all router variants, modifying only router-specific components (e.g., projection rank, scoring, or head design) when applicable.

Table 8. Key hyperparameters for OLMoE training.

Item	Value	Item	Value	Item	Value
$d_{\text{model}}$	2,048	Max sequence length	4,096	Experts $N$	64
Transformer layers $L$	16	Vocabulary size	50,280	Top- $k$	8
Attention heads $n_{\text{heads}}$	16	Load-balance weight $\lambda_{\text{bal}}$	0.01	Dropless routing	on
MLP ratio	1	Z-loss weight $\lambda_z$	0.001	Type	AdamW
Activation	SwiGLU	Learning rate	$4 \times 10^{-4}$	$(\beta_1, \beta_2)$	(0.9, 0.95)
Norm	RMSNorm	$\epsilon$	$10^{-8}$	Weight decay	0.1
Warmup tokens $t_{\text{warmup}}$	$3 \times 10^8$	Total tokens $t_{\text{max}}$	$10^{10}$	Decay	cosine
Global batch size	1024	Microbatch size	1	Distributed training	DDP

**Implementation Details.** All models are trained from scratch on the 10B-token in-distribution dataset described in Appendix E. We follow the standard OLMoE recipe with a Transformer backbone of  $d_{\text{model}} = 2048$ ,  $N = 64$  experts per MoE block, and top- $k = 8$  sparse activation. Optimization is performed using AdamW with cosine learning-rate decay, and all experiments are trained with Distributed Data Parallel (DDP) for scalability and stability. All runs are conducted on an 8× NVIDIA B200 (Blackwell) setup.

The original OLMoE implementation relies on Megablocks (Gale et al., 2023) for MoE kernel acceleration. However, Megablocks currently does not support Blackwell sm\_100 image configuration, which limits its compatibility on B200. To ensure correct execution and efficient expert dispatch, we replace the Megablocks MoE module with Tutel (Hwang et al., 2023), which offers architecture-agnostic kernels and stable performance under modern GPU backends. This change affects only the MoE dispatch backend and does not alter the routing logic or model formulation, ensuring fair and controlled comparisons across routing variants. For full reproducibility, we will release the complete configuration files and training scripts with the codebase.

### F.2. Training Configuration for ViT Experiments

This appendix reports the core training hyperparameters for ViT ImageNet experiments in Table 9. To isolate routing effects, we keep the backbone architecture, augmentation recipe, and optimization settings fixed across router variants, and only modify router-specific components (e.g., router type, rank, scoring mode, or head design) when applicable.

Table 9. Key hyperparameters for ViT-S ImageNet-1K training.

Item	Value	Item	Value	Item	Value
Model	ViT-S/16	Image size	224	#Classes	1000
ViT depth	12	Epochs	300	Batch size (per GPU)	128
Optimizer	AdamW	Learning rate	$5 \times 10^{-4}$	Min LR	$10^{-6}$
Weight decay	0.05	Warmup epochs	5	Grad clip	1.0
RandAugment	on	Random erasing prob.	0.25	Label smoothing	0.1
Mixup	0.8	CutMix	1.0		
Experts $N$	16	Top- $k$	2	MoE last- $n$ blocks	4
Aux. weight $\lambda_{\text{bal}}$	0.01	Learnable $\tau$	false		

## G. Full Experimental Results for OLMoE Experiments

*Table 10.* Downstream performance at the checkpoint closest to 10B total tokens (%). We report all four MMLU groups and their mean (MMLU), five additional tasks, and the overall mean (Overall) across nine tasks. Best results are in bold, and second-best results are underlined.

Method	H	Rank	Hum	Other	SocSci	STEM	MMLU	ARC-E	BoolQ	HSwag	PIQA	SciQ	Overall
X-MoE	-	32	23.4	<b>30.1</b>	25.8	19.1	24.6	<u>46.9</u>	60.0	<u>40.6</u>	<b>64.5</b>	68.8	<u>42.1</u>
Linear	-	-	22.3	21.5	27.0	19.9	22.7	<b>47.7</b>	60.0	38.7	61.1	66.8	40.5
L2R (Cosine)	-	2	22.3	27.3	30.1	19.9	24.9	42.2	61.1	<b>42.2</b>	60.0	<b>72.7</b>	42.0
L2R (Dot)	-	2	<u>25.4</u>	<u>30.9</u>	21.1	<u>20.3</u>	24.4	43.4	59.2	39.5	60.5	64.8	40.6
L2R (SIPS)	16	2	<b>28.9</b>	25.8	<b>34.8</b>	<b>21.1</b>	<b>27.6</b>	43.8	61.7	<u>40.6</u>	62.3	71.5	<b>43.4</b>
L2R (SIPS)	8	2	22.7	26.2	<u>32.0</u>	19.9	25.2	45.3	60.2	39.8	<u>64.3</u>	68.4	<u>42.1</u>
L2R (SIPS)	4	2	24.2	28.1	29.3	19.1	25.2	45.7	<u>62.1</u>	39.5	61.1	69.1	42.0
L2R (SIPS)	4	32	23.8	27.7	31.2	19.5	<u>25.6</u>	43.4	59.4	39.1	61.1	<u>71.9</u>	41.9
L2R (SIPS)	1	2	22.7	27.0	31.2	<b>21.1</b>	25.5	<u>46.9</u>	60.0	37.5	60.5	69.9	41.9
L2R (SIPS)	4	8	25.0	23.8	24.6	19.5	23.2	43.4	<b>62.3</b>	38.3	63.1	68.8	41.0

## H. Downstream Evaluation Protocol

We follow the downstream evaluation protocol used by OLMoE (Muennighoff et al., 2025) and OLMES (Gu et al., 2025) for reporting model quality. Specifically, we evaluate a fixed set of commonsense and knowledge benchmarks at checkpoints along training and report the average score (**Overall**) across all included tasks. All evaluations are performed using the same prompt format and normalization conventions as in the OLMoE/OLMES setup.

### H.1. Tasks and Metrics

Table 11 summarizes the tasks and evaluation settings used in this work. We report task accuracy for all benchmarks. For MMLU (Hendrycks et al., 2021), we follow the standard multiple-choice formulation and report both the mean MMLU score and the four group scores (Humanities, Social Sciences, STEM, Other) in Appendix G.

*Table 11. Summary of downstream evaluation.* We adopt the OLMoE/OLMES evaluation conventions. CF = completion/close (generative) formulation; MCF = multiple-choice formulation; Norm indicates the answer normalization used by the evaluator. ARC-E refers to ARC-Easy.

Dataset	Format	Norm	Metric
MMLU (Hendrycks et al., 2021)	MCF (5-shot)	char	Accuracy
ARC-E (Clark et al., 2018)	CF (0-shot)	none	Accuracy
BoolQ (Clark et al., 2019)	CF (0-shot)	none	Accuracy
HellaSwag (Zellers et al., 2019)	CF (0-shot)	char	Accuracy
PIQA (Bisk et al., 2020)	CF (0-shot)	char	Accuracy
SciQ (Welbl et al., 2017)	CF (0-shot)	none	Accuracy

### H.2. Early-Stage Evaluation

Our language MoE models are trained from scratch up to **10B tokens**. At this early pretraining stage, some downstream benchmarks commonly reported in OLMoE/OLMES (e.g., WinoGrande (Sakaguchi et al., 2020) and ARC-Challenge (Clark et al., 2018)) tend to exhibit high variance and unstable ranking across checkpoints, because the model has not yet formed sufficiently robust linguistic and commonsense representations. Including such tasks at 10B tokens can introduce noise that obscures routing-induced differences. Therefore, we focus on a compact set of tasks (Table 11) that are more stable and informative in the 10B-token regime, and we report an overall mean across these tasks for comparability.

### H.3. Benchmark Descriptions

We evaluate downstream quality using a compact suite of widely-used benchmarks that probe complementary capabilities (knowledge, reading comprehension, commonsense reasoning, and scientific QA). Below, we briefly describe each

benchmark and the associated evaluation interface used in our pipeline.

**MMLU.** Massive Multitask Language Understanding (MMLU) is a broad knowledge benchmark covering dozens of subjects spanning the humanities, social sciences, STEM, and other domains. Each example is a multiple-choice question with four candidate options. We evaluate MMLU in the standard multiple-choice formulation (MCF) and report accuracy. In addition to the overall MMLU mean, we optionally report the four group means (Hum, SocSci, STEM, Other) to diagnose capability skew across domains.

**ARC-E.** ARC-Easy (ARC-E) is a grade-school science QA benchmark focusing on relatively accessible science and commonsense questions. Each example provides a question and multiple candidate answers. Following prior work, we score candidates using conditional likelihood and select the best option, reporting accuracy. ARC-E tends to provide an early signal of improving general reasoning and basic scientific knowledge during pretraining.

**BoolQ.** BoolQ is a yes/no question answering benchmark grounded in short passages. Given a passage and a question, the model predicts a binary label (yes or no). We evaluate with accuracy. BoolQ emphasizes reading comprehension and entailment-style reasoning, and it is typically less sensitive to prompt formatting than many open-ended generation tasks.

**HellaSwag.** HellaSwag is a commonsense inference benchmark framed as sentence completion. Given a context, the model must choose the most plausible continuation from multiple candidates. We compute a score for each candidate continuation via conditional likelihood and report accuracy. HellaSwag probes grounded commonsense and causal/temporal plausibility, and is commonly used to reflect progress in event-level reasoning.

**PIQA.** PIQA tests physical commonsense reasoning for everyday situations. Each example describes a goal (e.g., how to accomplish a household task) and provides two candidate solutions; the model must select the more plausible one. We evaluate via candidate scoring and report accuracy. PIQA complements HellaSwag by focusing specifically on physical affordances and action feasibility.

**SciQ.** SciQ is a science QA dataset consisting of multiple-choice questions derived from science exams and accompanying explanations. We evaluate in the standard candidate-scoring setup and report accuracy. SciQ provides an additional view of science knowledge that is often more structured than ARC-style questions.

## I. Visualizations for OLMoE

### I.1. Visualizations for OLMoE Training Results

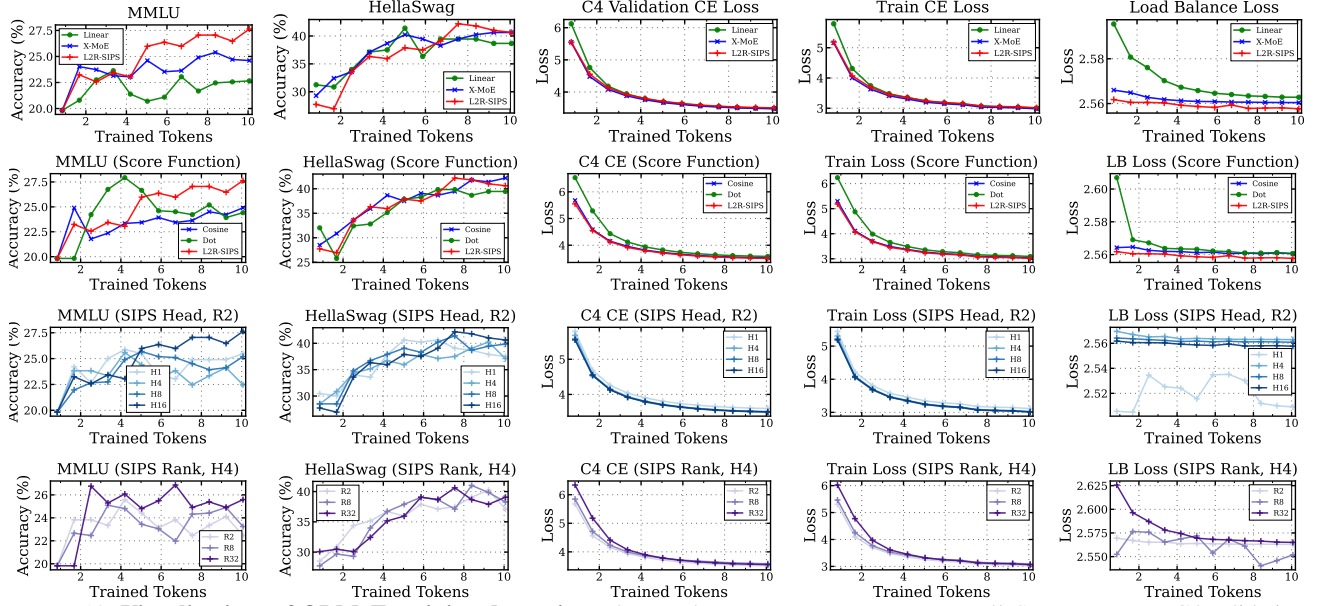


Figure 10. **Visualizations of OLMoE training dynamics.** The panels report MMLU accuracy, HellaSwag accuracy, C4 validation cross-entropy (CE), training CE, and load-balance loss across router variants. From top to bottom, we compare alternative methods, scoring modes, and ablations over head and rank settings. The x-axis denotes the number of trained tokens.

### I.2. Routing Geometry Visualizations in OLMoE

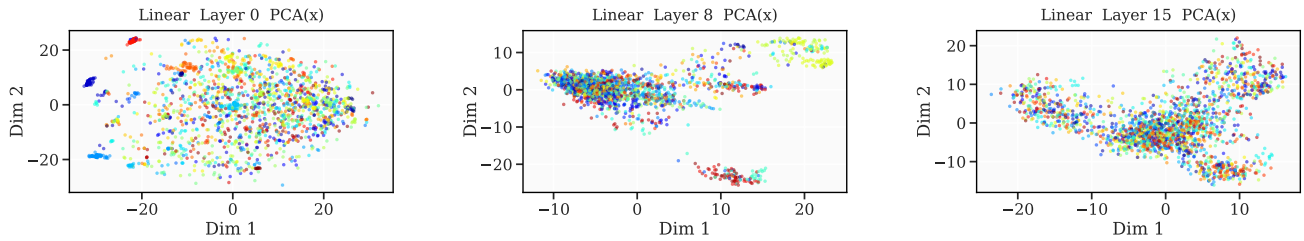
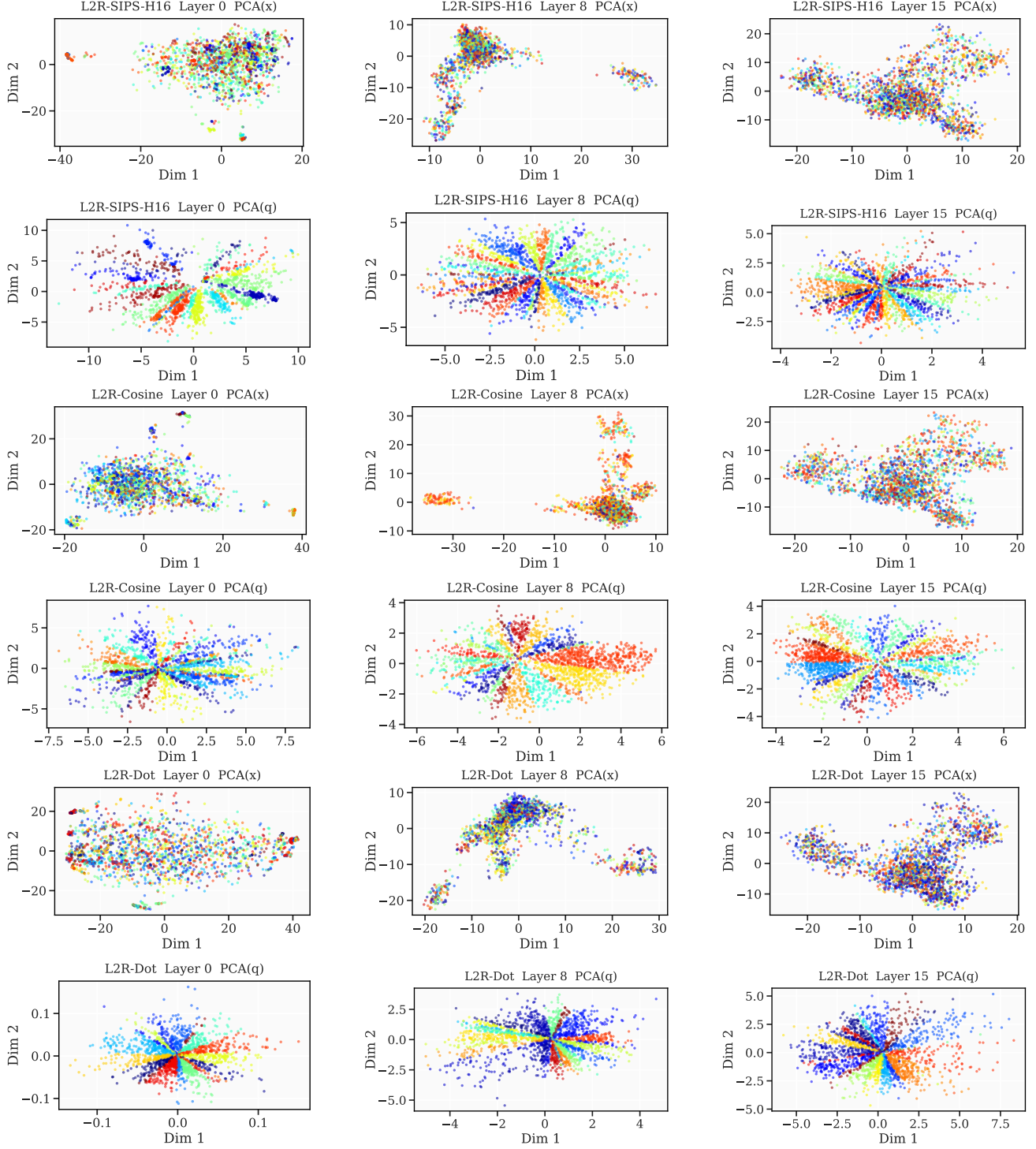
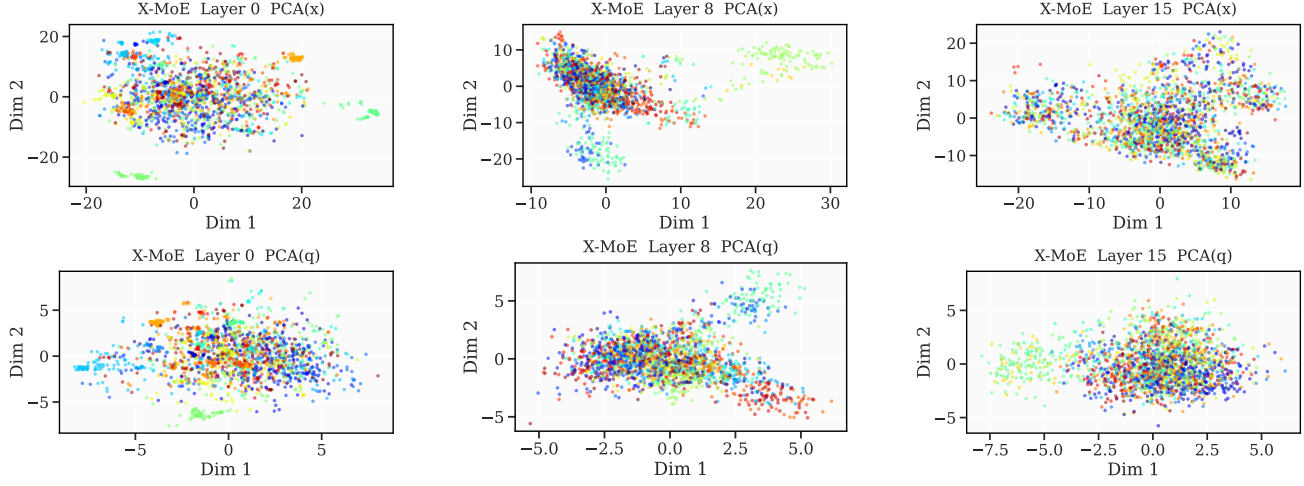


Figure 11. **Linear-router baselines.** PCA scatter plots in backbone representation space ( $x$ -space) for the same layers as Figure 12. Tokens are colored by the top-1 expert assignment under a linear router. These baselines help contrast expert separation in raw representations against our L2R latent routing space.

This section provides qualitative visualizations of routing geometry in the OLMoE setting. For selected MoE FFN layers (early-0; middle-8; late-15), we project token representations to two dimensions using PCA. Each point corresponds to a token representation and is colored by its top-1 routed expert. We visualize (i) the backbone representation space ( $x$ -space) and (ii) the routing latent space ( $q$ -space) produced by our low-rank projection. These plots support two observations: (1) routing in raw high-dimensional representations can lead to ambiguous expert separation, while (2) our routing latent space yields clearer cluster structure aligned with expert assignment, making the routing geometry more interpretable. We additionally report linear-router and X-MoE baselines for direct comparison.



**Figure 12. Routing geometry under L2R.** PCA scatter plots for three representative MoE FFN layers in OLMoE. Points are token representations colored by the top-1 expert. The first row shows backbone representations ( $x$ -space), and the second row shows routing latent queries ( $q$ -space). Compared to  $x$ -space, the  $q$ -space geometry typically exhibits clearer expert-aligned separation and reduced selection ambiguity.



**Figure 13. Routing geometry under the X-MoE router.** PCA projections of token representations at three FFN routing sites (blocks 0/8/15; left to right). Top: backbone activations in the raw representation space  $x$ . Bottom: router features  $q$  used for gating at the corresponding blocks. Each point denotes a token from the same evaluation batch (aggregated across distributed ranks), and colors indicate the selected top-1 expert. The visualization illustrates how token-to-expert partitioning evolves with depth and how separable the routed groups appear in  $x$  versus  $q$ .

### I.3. Expert Usage Heatmaps

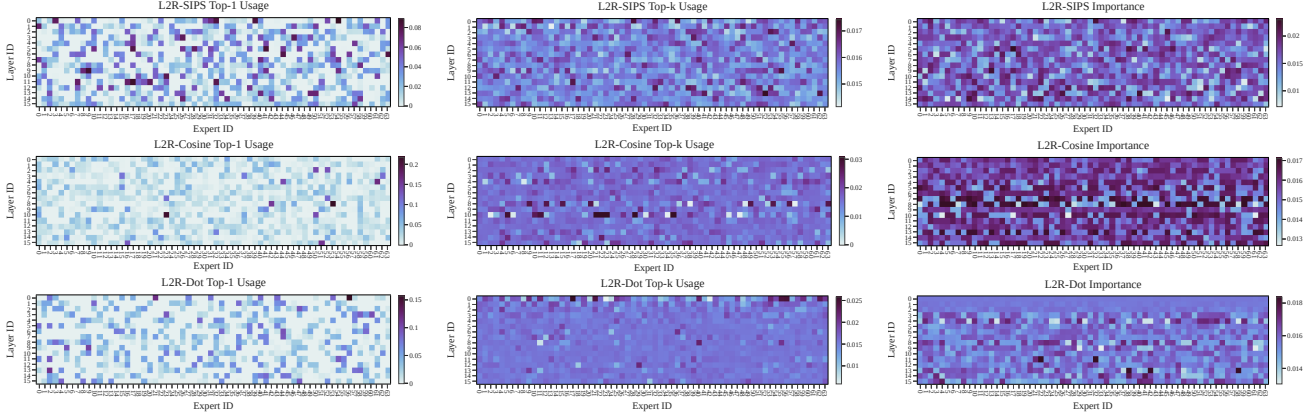


**Figure 14. Expert usage heatmaps for L2R-Cosine, L2R-Dot and L2R-SIPS.** From left to right: Top-1 routing frequency, Top-k routing frequency, and importance-based routing weights. Each row corresponds to a transformer layer and each column corresponds to an expert.

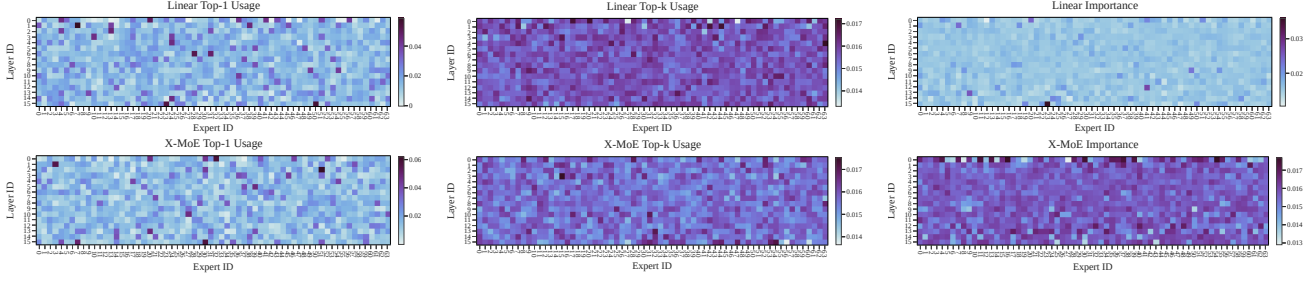


Figure 15. Expert usage heatmaps for Linear routing and X-MoE. From left to right: Top-1 routing frequency, Top-k routing frequency, and importance-based routing weights. Each row corresponds to a transformer layer and each column corresponds to an expert.

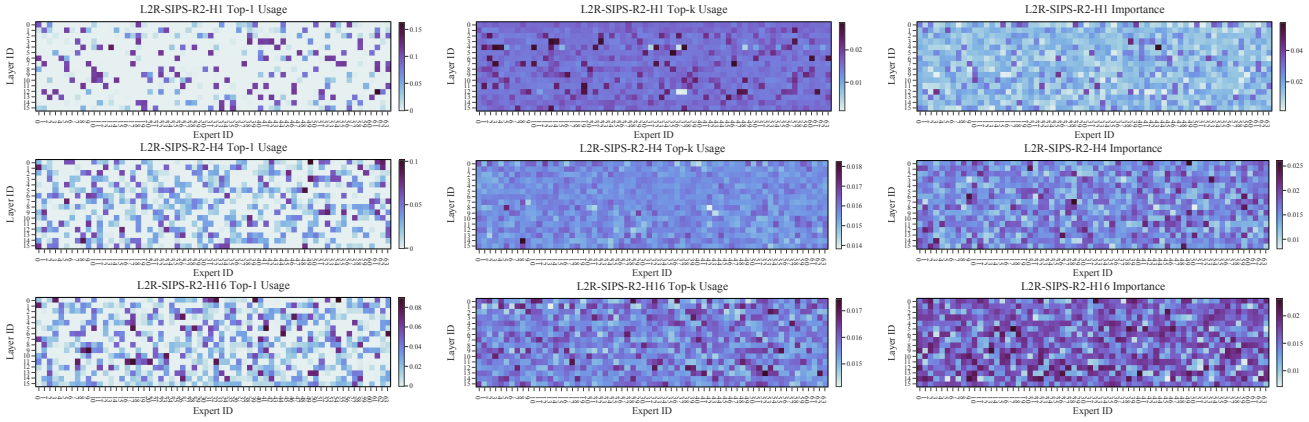


Figure 16. Expert usage heatmaps under different head settings in L2R-SIPS (Rank=2). From left to right: Top-1 routing frequency, Top-k routing frequency, and importance-based routing weights. Each row corresponds to a transformer layer, and each column corresponds to an expert.

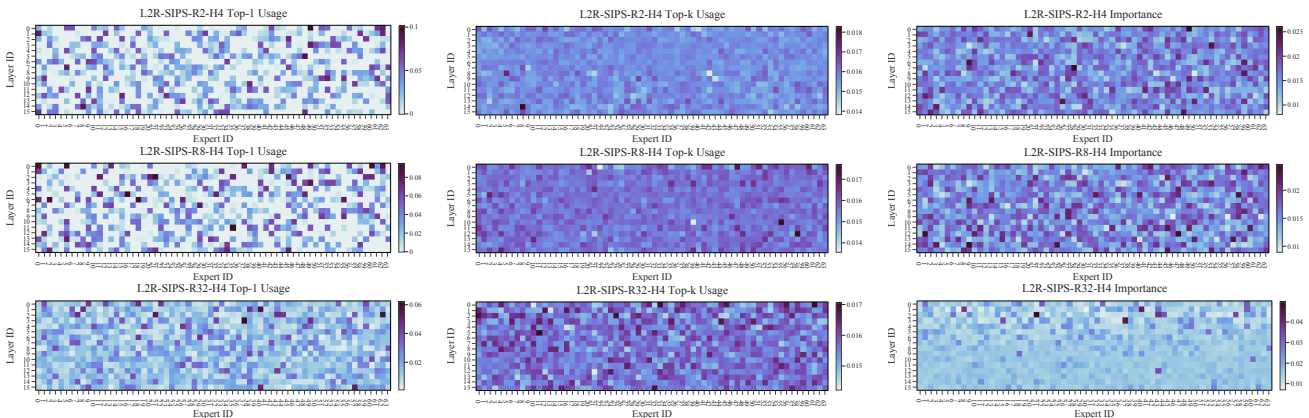


Figure 17. Expert usage heatmaps under different rank settings in L2R-SIPS (Head=4). From left to right: Top-1 routing frequency, Top-k routing frequency, and importance-based routing weights. Each row corresponds to a transformer layer, and each column corresponds to an expert.